JACS
JOURNAL OF THE AMERICAN CHEMICAL SOCIETY

Radically Enhanced Molecular Switches

Albert C. Fahrenbach,[1,3] Zhixue Zhu,[1] Dennis Cao,[1,3] Wei-Guang Liu,[4] Hao Li,[1] Sanjeev K. Dey,[1] Subhadeep Basu,[1] Ali Trabolsi,[1,5] Youssry Y. Botros,[2,6,7] William A. Goddard III,[3,4] and J. Fraser Stoddart[1,3*]

[1]*Department of Chemistry and* [2]*Department of Materials Science, Northwestern University 2145 Sheridan Road, Evanston, Illinois 60208, United States*

[3]*NanoCentury KAIST Institute and Graduate School of EEWS (WCU), Korea Advanced Institute of Science and Technology (KAIST), 373−1 Guseong Dong, Yuseong Gu, Daejeon 305−701 Republic of Korea*

[4]*Materials and Process Simulation Center, California Institute of Technology, Pasadena, California 91125, United States*

[5]*New York University Abu Dhabi, Center for Science and Engineering, Abu Dhabi, United Arab Emirates*

[6]*Intel Labs, Building RNB-6-61, 2200 Mission College Blvd. Santa Clara, CA, 95054-1549, United States*

[7]*National Center for Nano Technology Research, King Abdulaziz City for Science and Technology, P.O. Box 6086, Riyadh 11442, Kingdom of Saudi Arabia*

SUPPORTING INFORMATION

Table of Contents

S1. General Methods

The syntheses of the three [2]rotaxanes **R1**·6PF_6[S1], **R2**·6PF_6,[S1] **R3**·6PF_6[S1] and the [2]catenane **C1**·6PF_6[S2], have already been reported in the literature. UV/Vis spectra were recorded with UV-3600 Shimadzu spectrophotometer at 298 K unless otherwise noted. Nuclear magnetic resonance (NMR) spectra were recorded at 298 K on a Bruker Avance 500 spectrometer, with a working frequency of 500 MHz for ^{1}H. Variable temperature NMR experiments were recorded on a Bruker Avance 600 spectrometer with a working frequency of 600 MHz for ^{1}H. Chemical shifts are reported in ppm relative to the signal corresponding to the residual non-deuterated solvent (CD_3CN: δ 1.94 ppm; $(CD_3)_2CO$: δ 2.05 ppm). Cyclic voltammetry experiments (CV) experiments were carried out at room temperature unless otherwise noted in argon-purged solutions in MeCN with a Gamry Multipurpose instrument (Reference 600) interfaced to a PC. CV experiments were performed using a glassy carbon working electrode (0.071 cm^2, Cypress system). The electrode surface was polished routinely with 0.05 μm alumina-water slurry on a felt surface immediately before use. The counter electrode was a Pt coil and the reference electrode was a saturated calomel electrode. The concentration of the sample and supporting electrolyte tetrabutylammonium hexafluorophosphate (TBA·PF_6) were 1.0×10^{-3} mol L^{-1} and 0.1 mol L^{-1}, respectively. Experimental errors: potential values, +/– 10 mV. Digital simulations of the CV data was performed using DigiSim. Crystallographic data were collected at 100 K using a Bruker d8-APEX II CCD diffractometer (Cu Kα radiation, λ=1.54178 Å). Intensity data were collected using ω and φ scans spanning at least a hemisphere of reciprocal space for all structures (data were integrated using SAINT). Absorption effects were corrected on the basis of multiple equivalent reflections (SADABS). Structures were solved by direct methods (SHELXS) and refined by full-matrix least-squares against F^2 (SHELXL). Hydrogen atoms were assigned riding isotropic displacement parameters and constrained to idealized geometries.

S2. H^1 NMR Spectroscopy

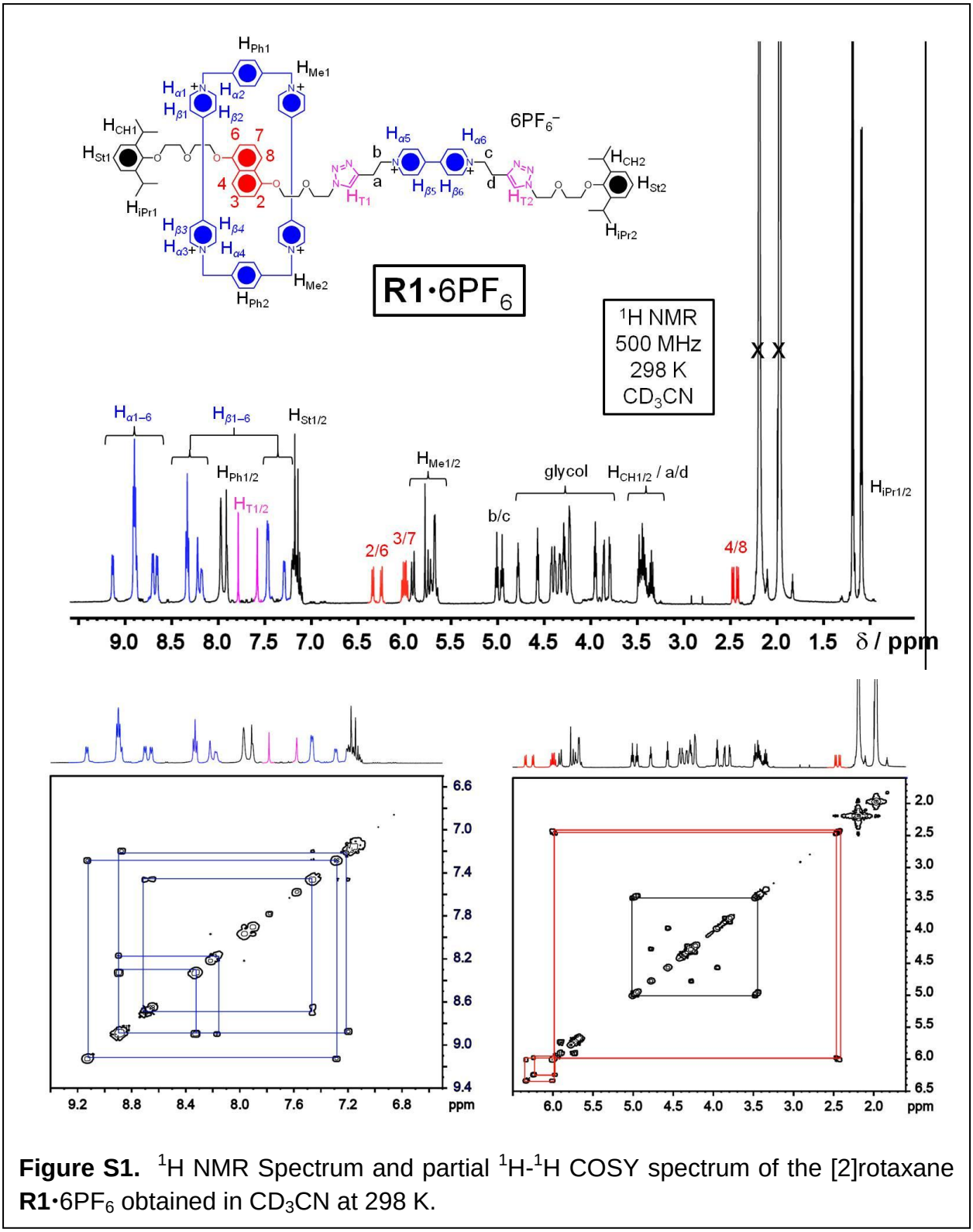

Figure S1. ^{1}H NMR Spectrum and partial ^{1}H-^{1}H COSY spectrum of the [2]rotaxane **R1**·6PF_6 obtained in CD_3CN at 298 K.

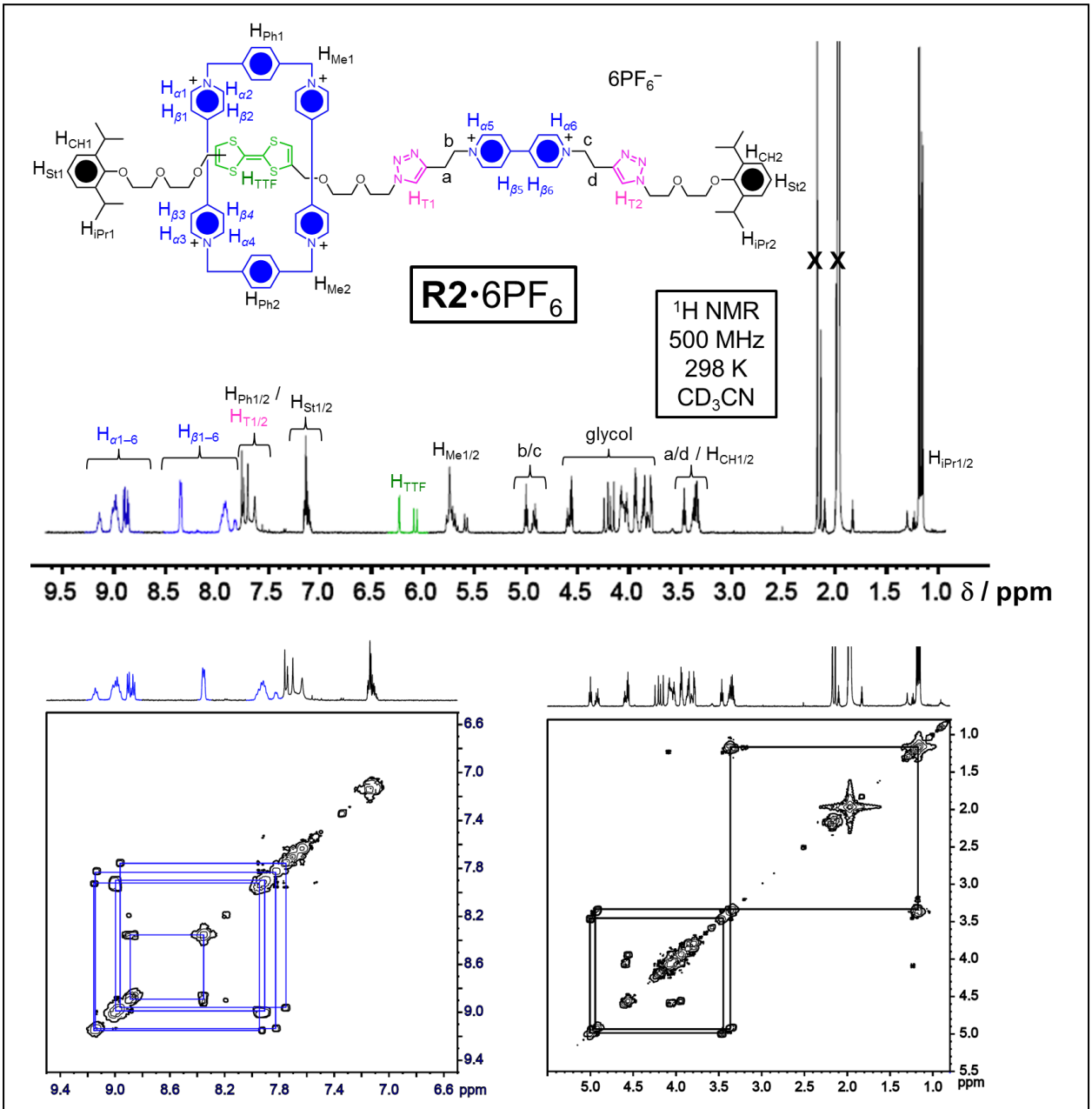

Figure S2. ^{1}H NMR Spectrum and partial ^{1}H-^{1}H COSY spectrum of the [2]rotaxane **R2**·6PF_6 obtained in CD_3CN at 298 K.

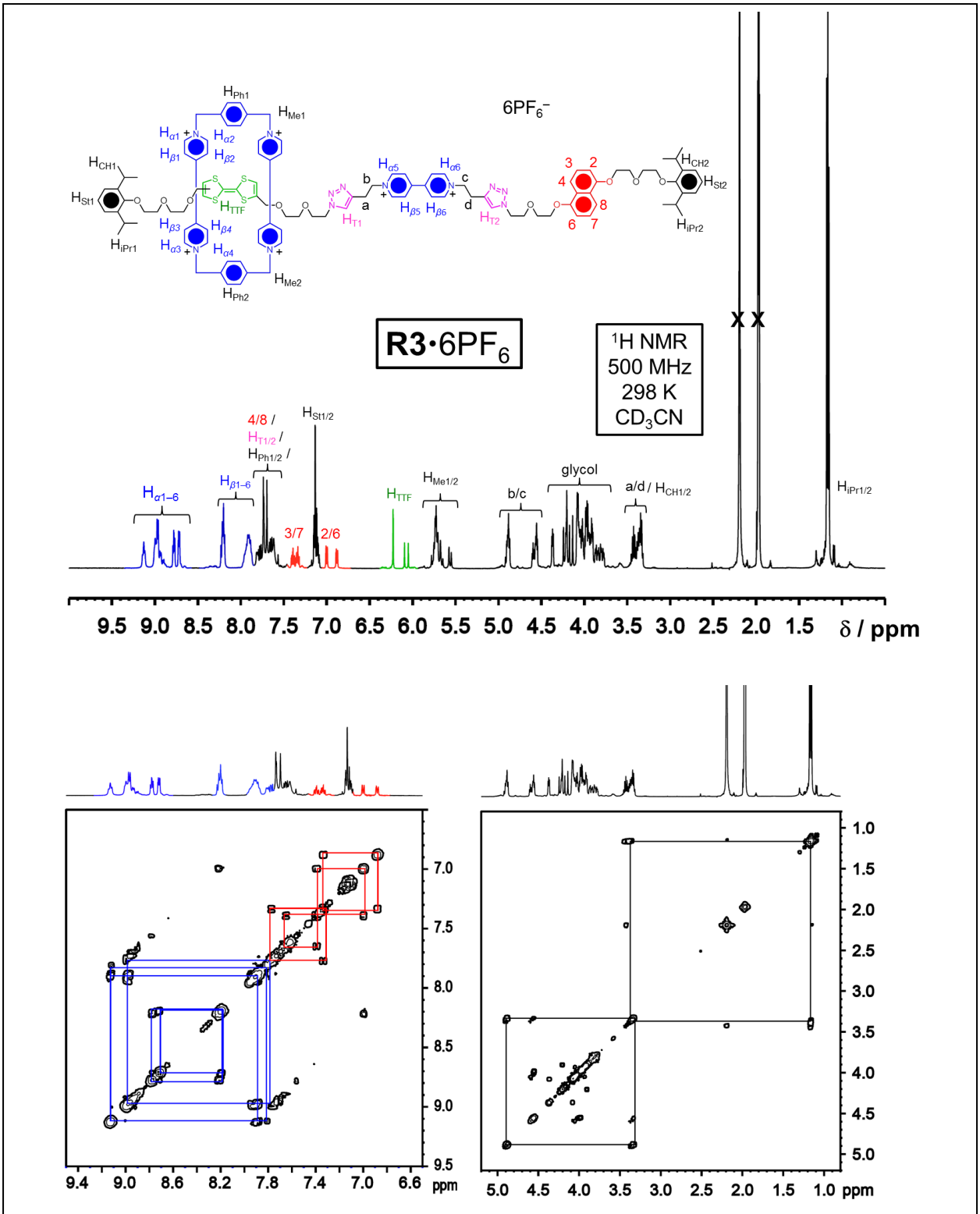

Figure S3. ^{1}H NMR Spectrum and partial ^{1}H-^{1}H COSY spectrum of the [2]rotaxane **R3**·6PF$_6$ in its GSCC obtained in CD$_3$CN at 298 K.

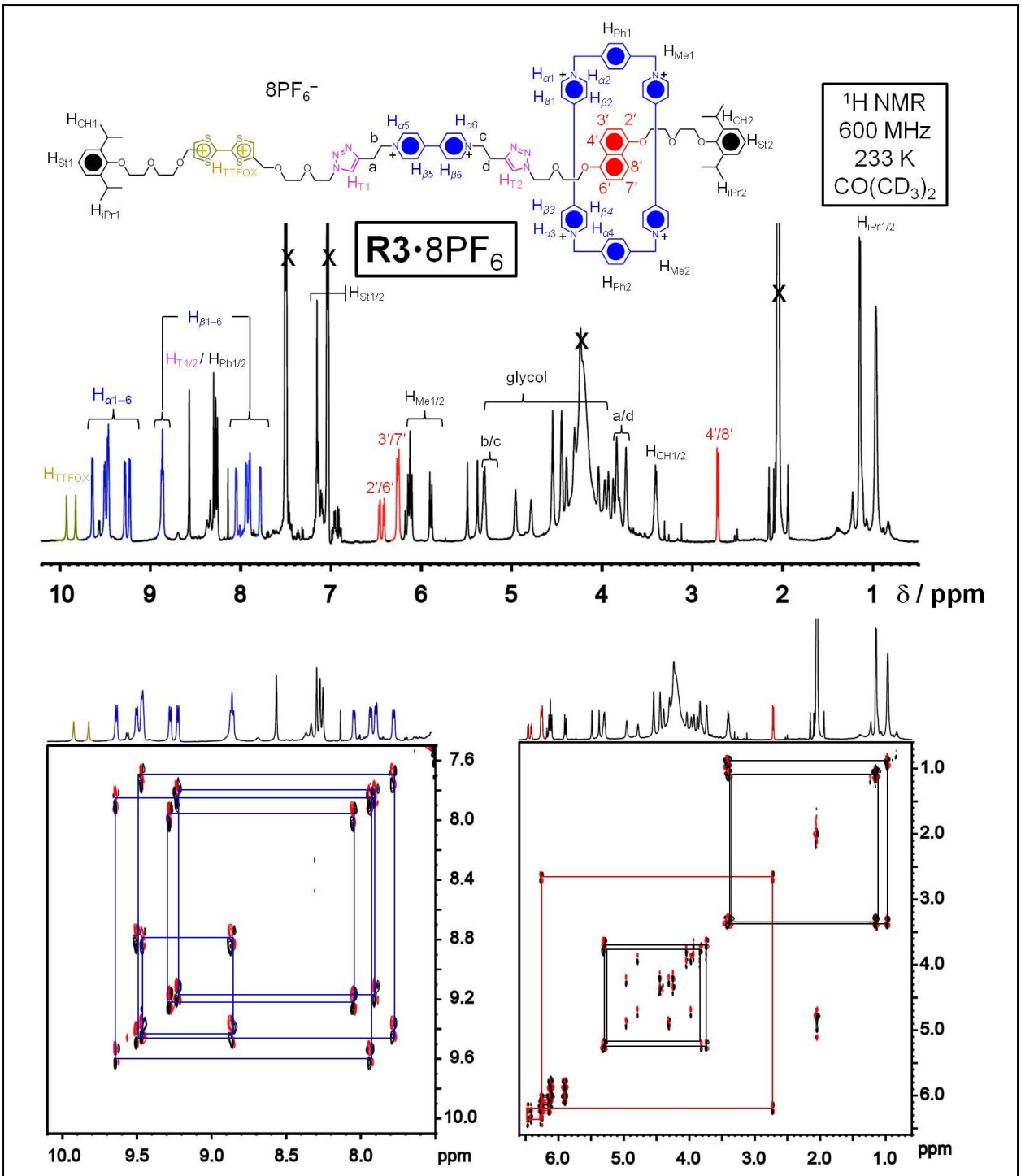

Figure S4. ^{1}H NMR Spectrum and partial ^{1}H-^{1}H COSY spectrum of the [2]rotaxane **R3**·8PF_6 following oxidation of its TTF unit to TTF^{2+} obtained in $(CD_3)_2CO$ at 233 K.

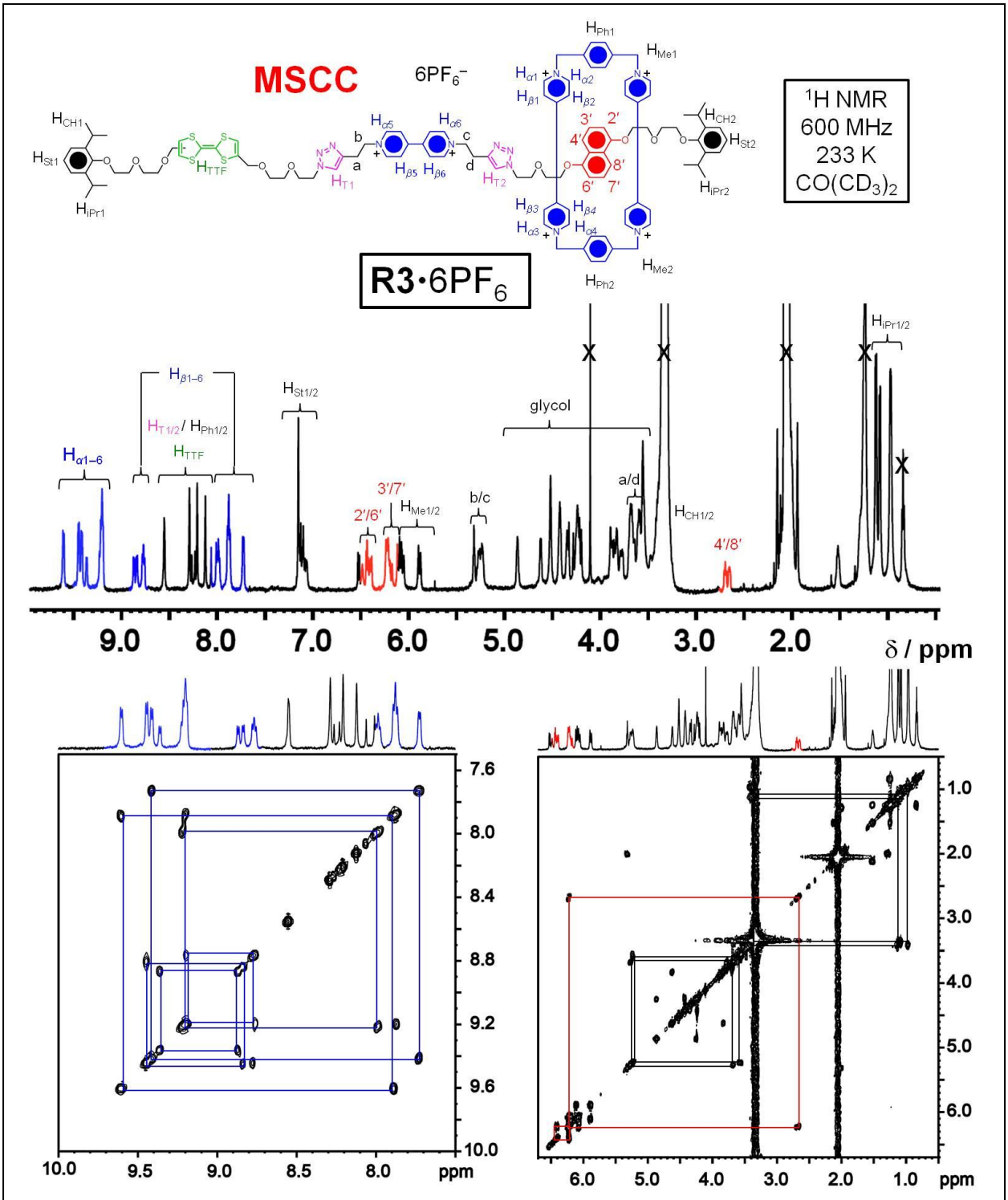

Figure S5. ^{1}H NMR Spectrum and partial ^{1}H-^{1}H COSY spectrum of the [2]rotaxane **R3**·6PF_6 in its MSCC obtained in $(CD_3)_2CO$ at 233 K.

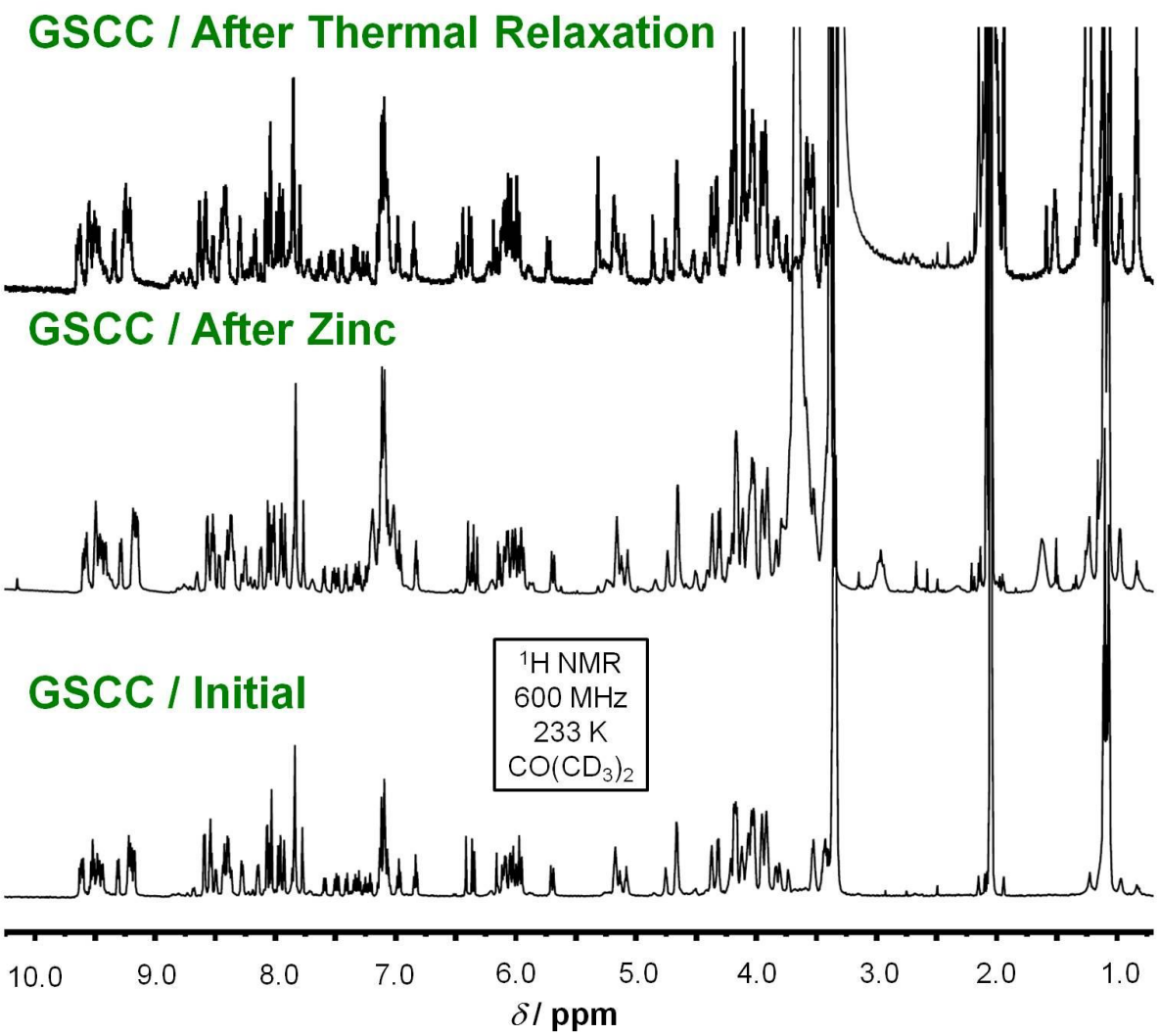

Figure S6. ^{1}H NMR Spectra of the rotaxane **R3**·6PF_6 in its GSCC recorded initially prior to any redox manipulation (bottom), after exposure of a solution of the MSCC to excess of zinc dust, followed by O_2 (middle), and after thermal relaxation of the MSCC to the GSCC.

S3. Cyclic Voltammetry and Digital Simulations

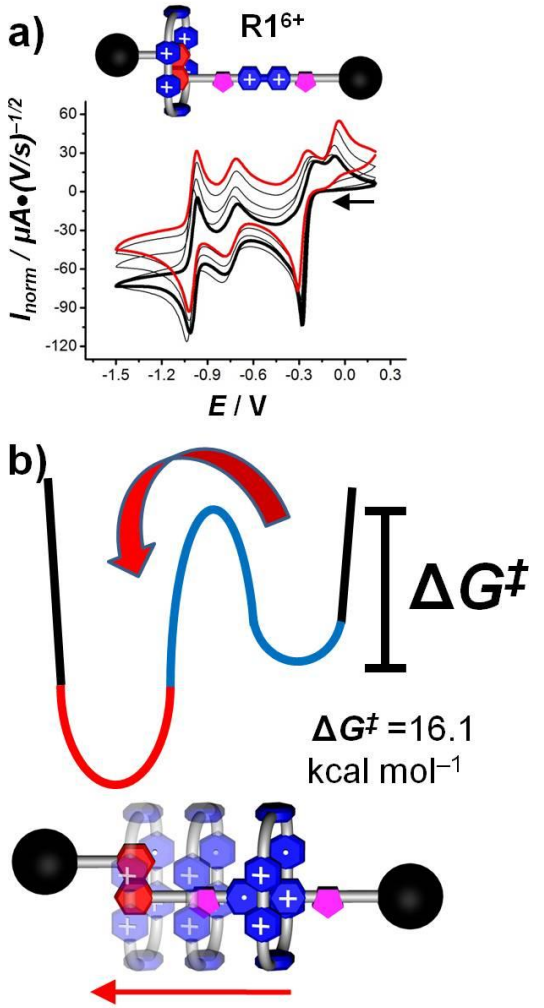

Figure S7. (a) Variable scan-rate CV data taken of the [2]rotaxane **R1**·6PF_6 in MeCN at 298 K. Black trace: 10 mV s^{-1}; Red trace: 500 mV s^{-1}. (b) Reaction coordinate diagram illustrating free energy barrier $\Delta G^{\ddagger}$ to shuttling of the $CBPQT^{(\bullet+)(2+)}$ ring. By comparing the experimental CV data to simulated data, a free energy barrier of 16.1 kcal mol^{-1} was determined.

The variable scan-rate CV data shown in Figure S7a was used to measure the free energy barrier to shuttling of the $CBPQT^{(\bullet+)(2+)}$ ring from the $BIPY^{\bullet+}$ to the DNP unit of the dumbbell component of **R1**·6PF_6 while in its bisradical tetracationic form. The CV data reveals that the electrochemical mechanism of switching for $\mathbf{R1}^{6+}$ is the same as that of the other MIMs described in this paper. (For a formal square-scheme mechanistic picture of this switching process, see Figure S10). By comparing the experimental CV data to simulated data based off the proposed mechanism, the rate of shuttling k_f was found to be 10 s^{-1} at 298 K, corresponding to a free energy barrier $\Delta G^{\ddagger}$ of 16.1 kcal mol^{-1}. Figure S7b shows a conceptual illustration of the reaction coordinate relating the shuttling motion of the $CBPQT^{(\bullet+)(2+)}$ ring to its associated free energy barrier. This data was then used to construct Figure 2 in the main text.

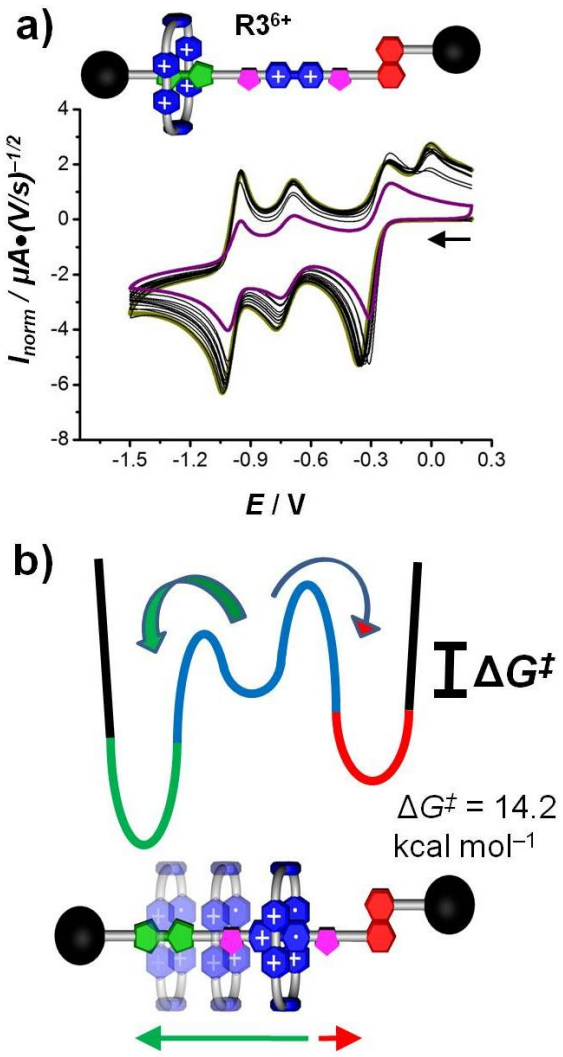

Figure S8. (a) Variable scan-rate CV data taken of the [2]rotaxane **R3**·6PF_6 in MeCN at 298 K. Purple trace: 200 mV s^{-1}; Gold trace: 1500 mV s^{-1}. (b) Reaction coordinate diagram illustrating free energy barrier $\Delta G^{\ddagger}$ to shuttling of the $CBPQT^{(\bullet+)(2+)}$ ring. By comparing the experimental CV data to simulated data, a free energy barrier of 14.2 kcal mol^{-1} was determined.

Figure S8a shows the variable scan-rate CV data obtained on the rotaxane **R3**·6PF_6 in the reductive region. This data reveals that the electrochemical mechanism of switching of $\mathbf{R3}^{6+}$ is the same as that of the other MIMs investigated in this article, with the added caveat that the $CBPQT^{(\bullet+)(2+)/4+}$ ring has an extra option in terms of what donor (TTF or DNP) to which it can shuttle. By comparing the experimental with the simulated data, we found that the rate of shuttling k_f of the $CBPQT^{(\bullet+)(2+)}$ ring from the $BIPY^{\bullet+}$ unit to the donor unit of the dumbbell component to be 250 s^{-1}, corresponding to a free energy barrier $\Delta G^{\ddagger}$ of 14.2 kcal mol^{-1} at 298 K. We propose that shuttling of the $CBPQT^{(\bullet+)(2+)}$ ring occurs in a mechanostereoselective fashion onto the TTF unit as a consequence of the much faster kinetics of this motion compared to the shuttling motion onto DNP. Figure S8b shows the conceptual reaction coordinate diagram illustrating this shuttling motion, shown in Figure 2 of the main text.

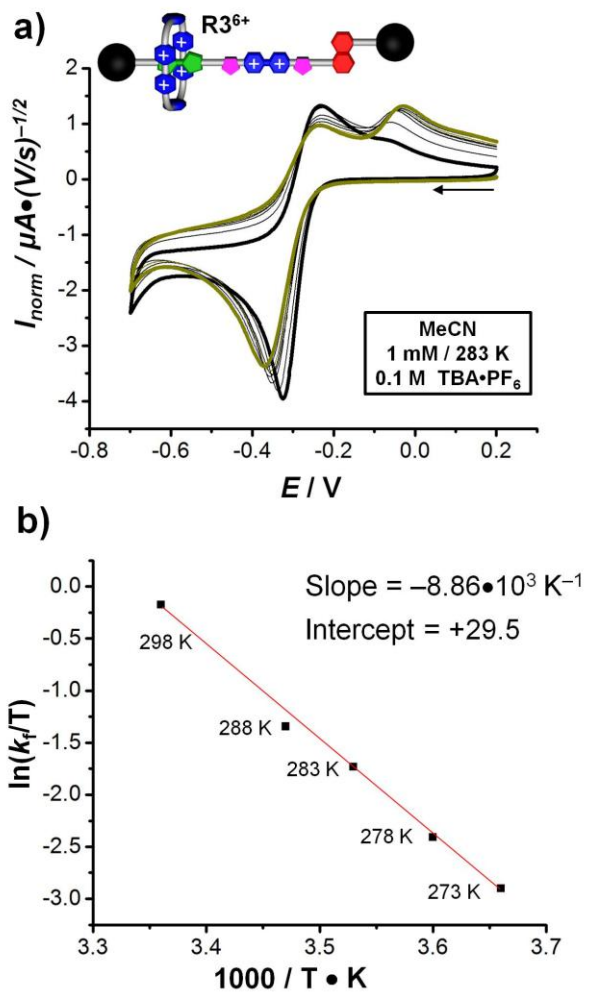

Figure S9. (a) Variable scan-rate CV data taken of the [2]rotaxane **R3**·6PF$_6$ in MeCN at 283 K. Purple trace: 200 mV s^{-1}; Gold trace: 1500 mV s^{-1}. (b) A plot of ln(k_f/T) versus inverse temperature using rate constants k_f for shuttling of the CBPQT$^{(\bullet+)2+}$ ring determined from the data obtained from variable scan-rate CV data as a function of temperature recorded on **R3**$^{6+}$. The slope of the best-fit line (red) is related to the enthalpic contribution $\Delta H^{\ddagger}$ and the intercept is related to the entropic contribution $\Delta S^{\ddagger}$ to the free energy barrier $\Delta G^{\ddagger}$ according to the linear form of the Eyring-Polanyi equation.

Figure S9a shows variable scan-rate CV data taken of the rotaxane **R3**·6PF$_6$ at 283 K. For the sake of experimental simplicity, the scan was only extended to –0.7 V, enough to access the trisradical form of the rotaxane. These same variable scan rate CV experiments were also performed at 298, 288, 278, and 273 K. In particular, the rate of shuttling k_f of CBPQT$^{(\bullet+)(2+)}$ ring from the BIPY$^{\bullet+}$ to the TTF unit was determined as a function of temperature by comparing the experimental CV data to digitally simulated CV data, and was found to decrease as the temperature was lowered. A plot of ln(k_f/T) versus 1/T (Figure S9b) at these different temperatures revealed a linear trend. Employing the linear form of the Eyring equation to a linear fit from these data points allowed us to calculate enthalpic contribution $\Delta H^{\ddagger}$ of +17.6 kcal mol^{-1} and an entropic contribution $\Delta S^{\ddagger}$ of +11.2 cal mol^{-1} K^{-1} to the free energy barrier $\Delta G^{\ddagger}$.

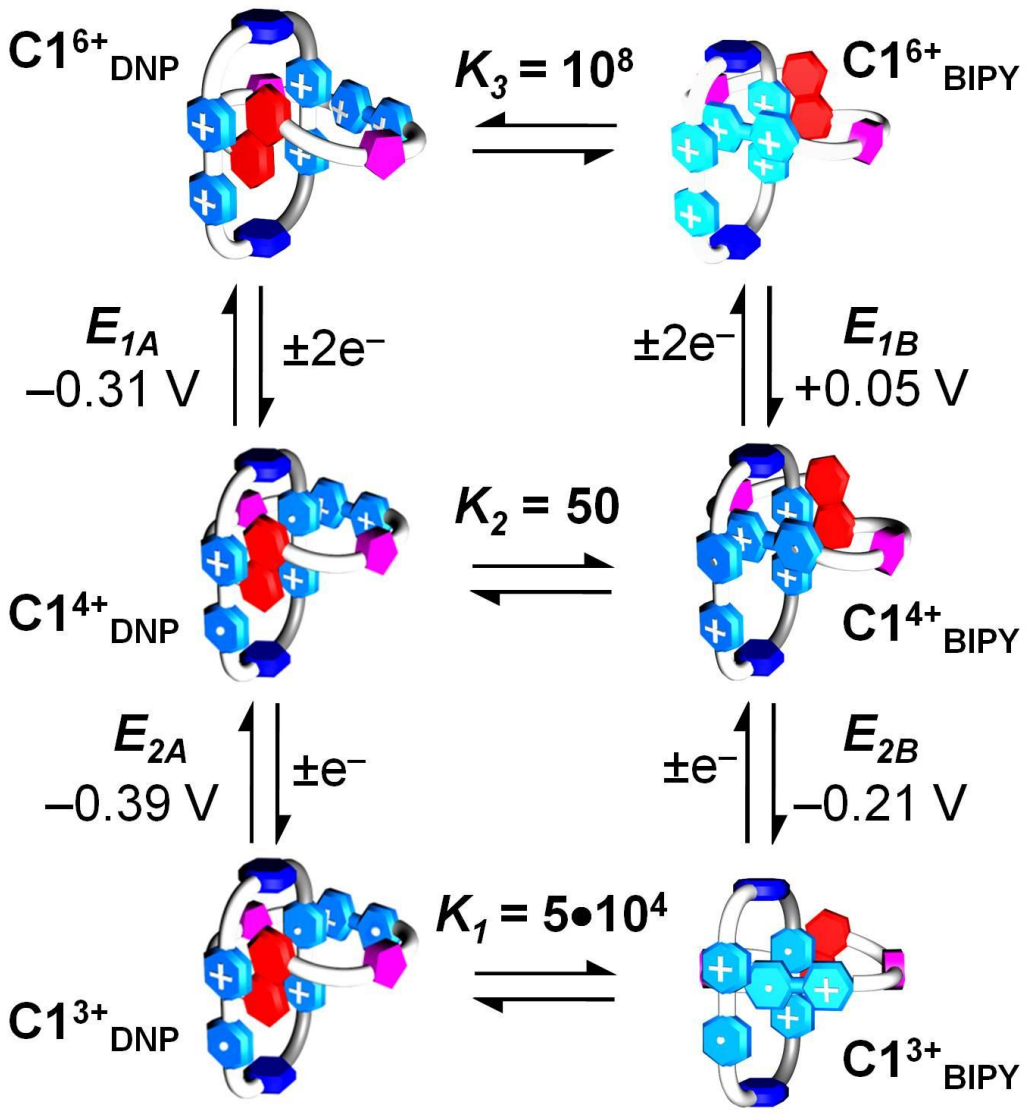

Figure S10. Formal square scheme mechanism of the proposed electrochemical switching behavior for the catenane **C1**·6PF_6 upon which digital simulations were modeled. The same square scheme mechanism was applied to the three rotaxanes **R1**·6PF_6, **R2**·6PF_6 and **R3**·6PF_6.

The square-scheme mechanism shown in Figure S10 for the catenane **C1**·6PF_6 was used to generate the simulated CV data shown in the main text according to the heterogeneous electron transfers and homogeneous chemical reactions shown below in Tables S1 and S2. This same mechanism was applied in the case of the three rotaxanes **R1**·6PF_6, **R2**·6PF_6 and **R3**·6PF_6. Table S3 lists the parameters that were used to generate the digitally simulated CV data, i.e., the same parameters used to conduct the CV experiments.

Table S1. Heterogeneous Electron Transfer Reactions

	Reaction	*E* / V
1	$C1^{6+}_{DNP} + 2e^- = C1^{4+}_{DNP}$	–0.31
2	$C1^{4+}_{DNP} + e^- = C1^{3+}_{DNP}$	–0.39
3	$C1^{6+}_{BIPY} + 2e^- = C1^{4+}_{BIPY}$	+0.05
4	$C1^{4+}_{BIPY} + e^- = C1^{3+}_{BIPY}$	–0.21
5	$C1^{3+}_{BIPY} + e^- = C1^{2+}_{BIPY}$	–0.77
6	$C1^{2+}_{BIPY} + e^- = C1^{0}_{BIPY}$	–1.00

Table S2. Homogenous Chemical Reactions

	Reaction	K_{eq}	k_f (s^{-1})	k_b (s^{-1})
7	$C1^{6+}_{BIPY} = C1^{6+}_{DNP}$	1.00×10^{8}*	1.0×10^{8} [b]	1.0×10^{-2}*
8	$C1^{4+}_{BIPY} = C1^{4+}_{DNP}$	0.02*	variable	variable
9	$C1^{3+}_{BIPY} = C1^{3+}_{DNP}$	2×10^{-5} [a]	20	1.00×10^{6} [a]

*Values were calculated automatically by the software.
[a]Experimental values.
[b]Assumed rate of formation constant based on ultra-fast decomplexation due to Coulombic repulsion.

Table S3. CV Parameters

E_{start} / V	E_{rev} / V	E_{end} / V	Area / cm^2	v / $V \cdot s^{-1}$
0.25	–1.5	0.25	0.071	VARIABLE

The values of the redox potentials shown in Table S1 were all determined from experimental CV data. The values of the redox potentials for Reactions **3** and **4** were estimated based on the potential of the oxidation peaks observed for these processes at faster scan rates. The value of the redox processes **1–6** were observed to differ only slightly from MIM to MIM. We determined previously[S3] the equilibrium constant associated with the inclusion of methyl viologen ($MV^{\bullet+}$) radical cation inside the cavity of the diradical dication $CBPQT^{2(\bullet+)}$ ring to be approximately $5 \cdot 10^4$ M^{-1}. We used this supramolecular complex $CBPQT^{2(\bullet+)} \subset MV^{\bullet+}$ as a model for the equilibrium, which occurs in the case of the MIMs studied in this article when in their trisradical forms, in order to generate the digitally simulated data. In particular, we used this same $5 \cdot 10^4$ value for the equilibrium constant governing reaction **9** as shown in Table S2, which defines in the trisradical redox state of **C1**$\cdot 6PF_6$ an equilibrium between a co-conformation which sees the $CBPQT^{2(\bullet+)}$ ring encircled around $BIPY^{\bullet+}$, i.e., the RSCC, and another co-conformation which sees the $CBPQT^{2(\bullet+)}$ ring encircled around DNP. The values of the equilibrium constants shown defined by reactions **7** and **8** in Table S2 are then calculated automatically by the software. The value of the rate constant k_f for reaction **7** was based on theoretical calculations performed[S4] on a similar situation involving the rate of shuttling of the $CBPQT^{4+}$ ring off of a dicationic TTF^{2+} unit. The value of the rate constants governing reaction **9** were again based on the rate constants for the model $CBPQT^{2(\bullet+)} \subset MV^{\bullet+}$ complex determined[S3] previously. The rate constants for reaction **9** were then varied in order to match the experimental variable scan rate data for all the MIMs.

S4. X-Ray Crystallography

Single crystals of $\mathbf{C1}^{2(\bullet+)(2+)}\bullet 4PF_6$ suitable for single-crystal X-ray crystallography were grown by slow-vapor diffusion under the inert conditions of a glove box. Excess of zinc dust was added to a solution of the $\mathbf{C1}\bullet 6PF_6$ in MeCN (~1 mM) and stirred for 30 min. The zinc dust was filtered from the solution using a 0.45 μm syringe-tip filter. Next, iPr$_2$O was allowed to vapor-diffuse into the MeCN solution at RT. After about a week, very dark single crystals were observed, which were the bisradical tetracationic $\mathbf{C1}^{2(\bullet+)(2+)}\bullet 4PF_6$.

Crystal data for $\mathbf{C1}^{2(\bullet+)(2+)}\bullet 4PF_6$: $C_{92}H_{108}F_{24}N_{16}O_9P_4$, M_r = 2169.33, triclinic, $P\bar{1}$, a = 15.2916(13), b = 26.090(2), c = 26.927(3) Å, α = 103.784(6)^o, β = 90.188(6)^o, γ = 99.938(5)^o, V = 10265.7 Å^3, T = 100(2) K, Z = 4, D_c = 1.404 g cm^{-3}, μ(Cu-Kα) 1.613 mm^{-1}, F(000) = 4496. Independent measured reflections 20948. R_1 = 0.1049, wR_2 = 0.2713 for 10743 independent observed reflections [$2\theta \leq 100.86^o$, $I > 2\sigma(I)$].

S5. Supplementary References

(S1) Trabolsi, A.; Khashab, N.; Fahrenbach, A. C.; Friedman, D. C.; Colvin, M. T.; Cotí, K. K.; Benitez, D.; Tkatchouk, E.; Olsen, J.-C.; Belowich, M. E.; Carmielli, R.; Khatib, H. A.; Goddard III, W. A.; Wasielewski, M. R.; Stoddart, J. F. *Nature Chem.* **2010**, *2*, 42.

(S2) Zhu, Z.; Fahrenbach, A. C.; Li, H.; Barnes, J. C.; Liu, Z.; Dyar, S. M.; Zhang, H.; Lei, J. Carmieli, R.,; Sarjeant, A. A.; Stern, C. L.; Wasielewski, M. R.; Stoddart, J. F. *J. Am. Chem. Soc.* **2012**, *134*, 11709.

(S3) Fahrenbach, A. C.; Barnes, J. C.; Lanfranchi, D. A.; Li, H.; Coskun, A.; Gassensmith, J. J.; Liu, Z.; Benitez, D.; Trabolsi, A.; Goddard, W. A. III; Elhabiri, M.; Stoddart, J. F. *J. Am. Chem. Soc.* **2012**, *134*, 3061

(S4) Kim, H.; Goddard III, W.A.; Jang, S.S.; Dichtel, W.R.; Heath, J.R.; Stoddart, J.F. *J. Phys. Chem. A* **2009**, *113*, 2136.